
A Ridgelet Approach to Poisson Denoising

Ali Dadras¹ Klara Leffler¹ Jun Yu¹

Abstract

This paper introduces a novel ridgelet transform-based method for Poisson image denoising. Our work focuses on harnessing the Poisson noise's unique non-additive and signal-dependent properties, distinguishing it from Gaussian noise. The core of our approach is a new thresholding scheme informed by theoretical insights into the ridgelet coefficients of Poisson-distributed images and adaptive thresholding guided by Stein's method.

We verify our theoretical model through numerical experiments and demonstrate the potential of ridgelet thresholding across assorted scenarios. Our findings represent a significant step in enhancing the understanding of Poisson noise and offer an effective denoising method for images corrupted with it.

1. Introduction

Image noise can be seen as a random variation within the image information. It is usually generated in the physical acquisition process and affects visual effects such as the image colour or brightness. Therefore, image denoising is a fundamental task in computer vision. The additive white Gaussian noise model is by far the most adopted. However, in imaging techniques where the acquisition process involves a counting process, the data are more accurately modelled by a Poisson distribution. Such processes occur in e.g. astronomy and astrophysics (Lantéri & Theys, 2005), spectral imaging (Priego et al., 2017), and biomedical imaging (Thanh & Dvoenko, 2015), including photon-counting imaging such as positron emission tomography and computed tomography (Vardi et al., 1985; Hasinoff, 2014; Thanh et al., 2019).

Assuming an image $\mathbf{X} = [X_{i,j}]$ follows a Poisson model, its pixel values are viewed as Poisson-distributed random variables. Hence, given a noiseless image Λ with pixel val-

ues $\lambda_{i,j} \geq 0$ at position (i, j) , the probability of observing a noisy pixel value $X_{i,j}$ is given by $X_{i,j} \sim \text{Po}(\lambda_{i,j})$ where

$$P(X_{i,j} = x) = \frac{\lambda_{i,j}^x e^{-\lambda_{i,j}}}{x!}, \quad (1)$$

where $(i, j) \in \mathbb{N}^N \times \mathbb{N}^M$. It is worth noting that Poisson noise is not additive and that its strength is directly dependent on the image intensity. From Equation (1), one can conclude that the signal-to-noise ratio (SNR) in each pixel is $\sqrt{\lambda_{i,j}}$, implying that lower intensity in observed images comes with stronger noise (Giryés & Elad, 2014; Zhang et al., 2019a). The mentioned SNR of the observed noisy Poisson image is proportional to the noiseless image (Zhang et al., 2021). Poisson noise substantially differs from Gaussian noise. With its direct dependency between signal and noise, it does not follow the simple additivity principle of white Gaussian noise. Furthermore, the variance is equal to the mean for Poisson-distributed variables, implying high variance for high-intensity levels. Therefore, traditional approaches for Gaussian noise removal do not directly apply to Poisson denoising (Thanh et al., 2019; Zhang et al., 2019b). Denoising of Poisson-distributed images aims at estimating the underlying noiseless intensity profile Λ from the noisy images \mathbf{X} . Therefore, defining the noise power in the image by its peak value, i.e., the maximum value of the underlying intensity profile Λ is natural.

1.1. Related Work

Methods for Poisson denoising can roughly be divided into two categories: direct and indirect. The indirect approaches are based on variance stabilisation transforms (VST) that remove the signal-dependency property such that an additive Gaussian model can approximate the noise. A classical Gaussian denoising approach can then be applied before inversely transforming the denoised image back to the original domain. The Anscombe (Anscombe, 1948) or Haar-Fisz (Fryzlewicz & Nason, 2004) transforms are the most commonly used. An extension of the Anscombe transform was presented incorporating multiscale VST that can be combined with thresholding in the wavelet, ridgelet or curvelet domains (Zhang et al., 2008). Combinations of VST and the popular Gaussian denoising technique of block-matching and 3D filtering have also been proposed for both high- and low-intensity data (Dabov et al., 2007; Azzari & Foi, 2016).

¹Department of Mathematics and Mathematical Statistics, Umeå University, Umeå, Sweden. Correspondence to: Ali Dadras <ali.dadras@umu.se>, Klara Leffler <klara.leffler@umu.se>.

The direct approaches aim to use the Poisson characteristics of the noise. Examples include total variation (TV) regularisation based on the gradient information of the image (Rudin et al., 1992). The TV-based approach encourages piecewise smoothness, exploiting that images often exhibit sharp transitions only at edges, allowing for effective noise reduction while preserving edges. Extensions into the Bayesian setting have been proposed, incorporating Poisson statistics into the data fidelity term (Le et al., 2007; Figueiredo & Bioucas-Dias, 2010). To overcome unwanted staircase effects resulting from the TV approaches, higher-order TV denoising was proposed (Chan et al., 2000). Sparsity-based regularisation has also been proposed, aiming to find the sparsest representation of a noisy image in terms of linear combinations of a dictionary of basis elements and reconstruct a clean image from the sparse representation. Examples include low-rank methods combined with sparse coding (Dong et al., 2012) and patch-based sparse representations combined with dictionary learning (Giryas & Elad, 2014).

Multiresolution strategies to Poisson intensity estimation were introduced to address potential correlations amongst the elements of \mathbf{X} . Statistical modelling of transform coefficients as latent variables, e.g. via filterbanks such as wavelets, is convenient since such transforms tend to generate temporal and spatial decorrelated coefficients as well as energy compaction properties for a variety of data (Hirakawa & Wolfe, 2012). Furthermore, the Poisson statistics are known to be preserved across scales in the low-pass channels of an unnormalised Haar wavelet transform (Luisier et al., 2010). Examples include generalised wavelet approaches with scale-dependent thresholds (Kolaczyk, 1996; 1999; Charles & Resson, 2003) and multiscale Bayesian approaches (Timmermann & Nowak, 1999; Lu et al., 2004). A Poisson unbiased risk estimator based on a linear expansion of thresholds (PURE-LET) was proposed following Stein’s unbiased risk estimator (SURE) for the Gaussian noise model (Luisier et al., 2010). There, the thresholds are adapted to local estimates of the signal-dependent noise variance derived from the corresponding low-pass coefficients at each scale. The same idea was also presented based on Poisson risk estimation via the Skellam distribution in a Bayesian setting (Hirakawa & Wolfe, 2012). As an alternative to pure wavelets and to better capture anisotropic features such as lines, the Ridgelet transform was proposed (Candès & Donoho, 1999), moving the wavelet analysis into the Radon domain. Implementations of the ridgelet transform are based on either the finite Radon transform (Do & Vetterli, 2000) or radial discrete lines in the Fourier domain (Carre & Andres, 2004). Poisson denoising via ridgelet transform has been implemented via integration of dual-tree complex wavelet transform of the radon coefficients (Chen & Kégl, 2007), geometric multiscale ridgelet support vector transform (Yang et al., 2013), and patchwise finite ridgelet

transform (Liu et al., 2014).

Apart from the model-based methods described above, recent developments in learning have motivated data-driven approaches to address the Poisson noise. Motivated by the traditional VST methods, three convolutional neural subnetworks were employed to simulate the forward transform, the Gaussian denoising, and the inverse transform via the so-called VST-Net (Zhang et al., 2019b). Direct learning strategies that focus on the Poisson characteristics have, for instance, taken inspiration from Gaussian image denoising, e.g. the trainable nonlinear reaction-diffusion model for Gaussian denoising of images (Chen & Pock, 2016), where an extension was presented for fast and accurate Poisson denoising, replacing the reaction term by a Poisson noise-derived function (Feng et al., 2017). A deep convolutional denoising network (DenoiseNet) was proposed for low-light images (Remez et al., 2017). An improvement to deep convolutional neural networks was also presented with additional multi-directional long-short-term memory networks to better capture and learn the statistics of the residual noise components (Kumwilaisak et al., 2020). Recently, a variational Bayesian deep network was proposed for blind Poisson denoising, combining subnetworks for noise estimation and removal (Liang et al., 2023).

1.2. Contribution and Outline

We aim to develop a novel approach for Poisson denoising based on the ridgelet transform. In this paper we, therefore, investigate the distributional properties of the noisy image in its ridgelet domain and propose a proper thresholding scheme for noise removal. The manuscript is structured as follows. In Section 2 we derive the distribution of the ridgelet coefficients; and in Section 3 we perform numerical experiments to verify the theoretically derived distributions and illustrate the potential of ridgelet thresholding. We conclude in Section 4 with some discussion.

2. Theory and Methods

In this section, we will investigate the distributional properties of the ridgelet coefficients of the Poisson-distributed image.

We model the image data as

$$\mathbf{X} = \mathbf{T}(\Lambda) \tag{2}$$

where \mathbf{X} is a matrix of measurements, Λ is a noiseless data matrix, and $\mathbf{T}(\cdot)$ is a signal dependent Poisson matrix with $\mathbb{E}[\mathbf{T}(\Lambda)] = \Lambda$.

2.1. Preliminaries

The ridgelet transform was introduced in 1999 as a geometrical generalisation of wavelets, applying one-dimensional wavelet transforms to projections in the Radon domain (Candès & Donoho, 1999). For this study to be self-contained, we include some preliminary theories about the Radon and ridgelet (wavelet) transforms.

2.1.1. THE RADON TRANSFORM

The Radon Transform in its continuous form is a fundamental operation in image processing, e.g. computed tomography (CT) and positron emission tomography (PET). It involves integrating an image function $f(\mathbf{s})$ along straight lines in the plane. Each line is uniquely defined by its perpendicular distance $r \in (-\infty, \infty)$ from the origin and the angle $\theta \in [0, \pi)$ the line makes with the horizontal axis. Mathematically, the Radon transform can be expressed as

$$\mathbb{R}_f(r, \theta) = \int_{\mathbb{R}^2} f(\mathbf{s}) \delta(s_1 \cos \theta + s_2 \sin \theta - r) ds$$

where δ represents the Dirac delta function. By varying r and θ , the Radon transform captures the global structure of $f(\mathbf{s})$ from different perspectives. Since the Radon transform transforms a point δ -function in f into a sinusoidal line δ -function in \mathbb{R}_f , the transform function is often referred to as a sinogram (Press, 2006). The inverse Radon transform is utilised in PET imaging to reconstruct cross-sectional images from sinogram projections.

2.1.2. THE RIDGELET TRANSFORM

The ridgelet transform is built on combining the Radon and wavelet transforms. The (separable) continuous wavelet transform of a signal $f(\mathbf{s}) \in L^2(\mathbb{R})$ at scales \mathbf{a} and locations \mathbf{b} is defined by

$$W(\mathbf{a}, \mathbf{b}) = \int_{\mathbb{R}^2} f(\mathbf{s}) \psi_{\mathbf{a}, \mathbf{b}}(\mathbf{s}) ds,$$

where the wavelet functions in two dimensions are tensor products

$$\psi_{\mathbf{a}, \mathbf{b}}(\mathbf{s}) = \psi_{a_1, b_1}(s_1) \psi_{a_2, b_2}(s_2)$$

of one-dimensional scaled and shifted wavelet functions $\psi_{a,b}(t) = a^{-1/2} \psi((t-b)/a)$, for $a > 0$ and $b \in \mathbb{R}$.

Given its construction, the basic strategy for calculating the continuous ridgelet transform is first to compute the Radon transform and then apply a one-dimensional wavelet transform to the Radon projections $\mathbb{R}_f(\theta, \cdot)$, i.e.

$$R(a, b, \theta) = \int_{\mathbb{R}} \mathbb{R}_f(r, \theta) \psi_{a,b}(r) dr.$$

2.2. Distribution of wavelet coefficients

When operating the different transforms on the image data, their discrete versions are applied.

The discrete wavelet transform of a vector $\mathbf{x} \in \mathbb{N}^N$ is based on the discretised version of a wavelet function ψ at scale j and location k . The wavelet coefficient $W_{j,k}$ of $\mathbf{x} = (x_1, \dots, x_N)$ at (j, k) is then the projection of \mathbf{x} onto a wavelet $\psi_{j,k}$, given as an inner product (Jensen & la Cour-Harbo, 2001) by

$$W_{j,k} = \sum_i \psi_{j,k}[i] * x_i. \quad (3)$$

Theorem 2.1 (Distribution of wavelet coefficients). *Let $\mathbf{x} \in \mathbb{N}^N$ be a vector of independent Poisson random variables x_i with intensities λ_i . The distribution of the discrete wavelet coefficients $W_{j,k}$ of \mathbf{x} can be approximated by the distribution $\mathcal{S}(\tilde{\lambda}_{j,k}^+, \alpha_{j,k}^+, \tilde{\lambda}_{j,k}^-, \alpha_{j,k}^-)$ that is the distribution of the scaled Poisson differences $W_{j,k} = \alpha_{j,k}^+ \tilde{W}_{j,k}^+ - \alpha_{j,k}^- \tilde{W}_{j,k}^-$ where $\tilde{W}_{j,k}^\pm$ are Poisson variables with intensities $\tilde{\lambda}_{j,k}^\pm$ and*

$$\tilde{\lambda}_{j,k}^\pm = \frac{\left(\sum_{i \in \mathcal{I}_{j,k}^\pm} \lambda_i \psi_{j,k,i} \right)^2}{\sum_{i \in \mathcal{I}_{j,k}^\pm} \lambda_i (\psi_{j,k,i})^2}$$

$$\alpha_{j,k}^\pm = \frac{\sum_{i \in \mathcal{I}_{j,k}^\pm} \lambda_i (\psi_{j,k,i})^2}{\sum_{i \in \mathcal{I}_{j,k}^\pm} \lambda_i |\psi_{j,k,i}|}.$$

where $W_{j,k} = \sum_i \psi_{j,k,i} x_i$ as defined in Equation (3) and we define $\mathcal{I}_{j,k}^+ = \{i | \psi_{j,k,i} \geq 0\}$ and $\mathcal{I}_{j,k}^- = \{i | \psi_{j,k,i} < 0\}$.

Proof. We begin by splitting Equation (3) into two parts

$$W_{j,k} = W_{j,k}^+ - W_{j,k}^-,$$

where

$$W_{j,k}^+ = \sum_{i \in \mathcal{I}_{j,k}^+} \psi_{j,k,i} x_i$$

$$W_{j,k}^- = \sum_{i \in \mathcal{I}_{j,k}^-} |\psi_{j,k,i}| x_i,$$

where for any i in $\mathcal{I}_{j,k}^+$, $\psi_{j,k,i}$ is positive, and for any i in $\mathcal{I}_{j,k}^-$ is negative.

Note that $W_{j,k}^+$ and $W_{j,k}^-$ are the sum of weighted Poisson variables. Let us compute the mean and variance of $W_{j,k}^+$ and $W_{j,k}^-$

$$\mu_{W_{j,k}^+} = \sum_{i \in \mathcal{I}_{j,k}^+} \lambda_i \psi_{j,k,i}, \quad \mu_{W_{j,k}^-} = \sum_{i \in \mathcal{I}_{j,k}^-} \lambda_i |\psi_{j,k,i}|$$

$$\sigma_{W_{j,k}^+}^2 = \sum_{i \in \mathcal{I}_{j,k}^+} \lambda_i \psi_{j,k,i}^2, \quad \sigma_{W_{j,k}^-}^2 = \sum_{i \in \mathcal{I}_{j,k}^-} \lambda_i \psi_{j,k,i}^2$$

Using the properties of scaled Poisson distribution (SPD) (Bohm & Zech, 2014), we can approximate the distributions with the distribution of scaled Poisson random variables $\hat{W}_{j,k}^+ := \alpha_{j,k}^+ \tilde{W}_{j,k}^+$ and $\hat{W}_{j,k}^- := \alpha_{j,k}^- \tilde{W}_{j,k}^-$ where $\tilde{W}_{j,k}^+ \sim \text{Po}(\tilde{\lambda}_{j,k}^+)$ and $\tilde{W}_{j,k}^- \sim \text{Po}(\tilde{\lambda}_{j,k}^-)$. We use moment matching to find the best parameters for $\hat{W}_{j,k}$

$$\begin{aligned}\mu_{\hat{W}_{j,k}^+} &= \alpha_{j,k}^+ \tilde{\lambda}_{j,k}^+ = \sum_{i \in \mathcal{I}_{j,k}^+} \lambda_i \psi_{j,k,i} \\ \mu_{\hat{W}_{j,k}^-} &= \alpha_{j,k}^- \tilde{\lambda}_{j,k}^- = \sum_{i \in \mathcal{I}_{j,k}^-} \lambda_i |\psi_{j,k,i}| \\ \sigma_{\hat{W}_{j,k}^+}^2 &= (\alpha_{j,k}^+)^2 \tilde{\lambda}_{j,k}^+ = \sum_{i \in \mathcal{I}_{j,k}^+} \lambda_i \psi_{j,k,i}^2 \\ \sigma_{\hat{W}_{j,k}^-}^2 &= (\alpha_{j,k}^-)^2 \tilde{\lambda}_{j,k}^- = \sum_{i \in \mathcal{I}_{j,k}^-} \lambda_i \psi_{j,k,i}^2.\end{aligned}$$

This will give us the parameters of SPDs.

$$\begin{aligned}\tilde{\lambda}_{j,k}^\pm &= \frac{\left(\sum_{i \in \mathcal{I}_{j,k}^\pm} \lambda_i \psi_{j,k,i} \right)^2}{\sum_{i \in \mathcal{I}_{j,k}^\pm} \lambda_i (\psi_{j,k,i})^2} \\ \alpha_{j,k}^\pm &= \frac{\sum_{i \in \mathcal{I}_{j,k}^\pm} \lambda_i (\psi_{j,k,i})^2}{\sum_{i \in \mathcal{I}_{j,k}^\pm} \lambda_i |\psi_{j,k,i}|}.\end{aligned}$$

This completes the proof. \square

2.3. Discrete Radon transform

In this sub-section, we would like to calculate the distribution of the discrete Radon transform. Dealing with discrete data, there is a vast number of discrete versions of the Radon transform (DRT).

2.3.1. DISCRETE APPROXIMATIONS OF LINES

In order to compute the discrete Radon transform, we need to define the discrete approximations of lines. Here one can use different line definitions such as Götz-Druckmüller-Brady approach or rotation based line definition to approximate lines (Götz & Druckmüller, 1996; Brady, 1998). The DRT algorithm sums an image's pixel values along a set of aptly chosen discrete lines, complete in slope and intercept. Different line approximations come with different computational complexities and approximation errors. For an image of size $N \times N$, Götz-Druckmüller-Brady algorithm has a computational complexity of $\mathcal{O}(N^2 \log(N))$. This method approximates a continuous line with intercept h and slope $s/(N-1)$. One can show that its maximum vertical deviation from the continuous line is less than or equal to $\frac{1}{6} \log_2(N)$ (Brady, 1998).

Let $\mathbf{X} = [X_{i,j}]$ be an image matrix of size N , we define a set of lines $\mathcal{D}_N(h, s)$ that transect the image, passing exactly through one array point in each column of the array and parameterised by integers h and s .

Equipped with these discrete line definitions, we can define the DRT as follows

$$R_{\mathbf{X}}(h, s) = \sum_{(i,j) \in \mathcal{D}_N(h,s)} X_{i,j},$$

where we assume $X_{i,j} = 0$ if i or j is outside the range $[0, N-1]$.

2.3.2. DISTRIBUTION OF RADON TRANSFORM

Using the DRT defined in the previous part, we can calculate the distribution of the DRT.

Theorem 2.2 (Distribution of the DRT). *Let \mathbf{X} be a random matrix with Poisson distributed entries with intensities $\lambda_{i,j}$ for each entry. The discrete Radon transform $R_{\mathbf{X}}(h, s)$ of \mathbf{X} have Poisson distribution with the following intensity*

$$\lambda_{h,s} = \sum_{(i,j) \in \mathcal{D}_N(h,s)} \lambda_{i,j}$$

Proof. *It is clear that $R_{\mathbf{X}}(h, s)$ is the sum of Poisson random variables with intensity $\lambda_{i,j}$ where $\{(i, j) \in \mathcal{D}_N(h, s)\}$, therefore, it is Poisson distributed with intensity $\lambda_{h,s} := \sum_{(i,j) \in \mathcal{D}_N(h,s)} \lambda_{i,j}$.* \square

2.4. Distribution of Ridgelets

Combining the result from Section 2.3 and Section 2.2, we can derive the distribution of the Ridgelet coefficients. Ridgelets are defined as the wavelet transform of the Radon transform of the data with fixed slopes, say s .

Theorem 2.3 (Distribution of Ridgelet coefficients). *Let \mathbf{X} be a random matrix with independent Poisson distributed entries with intensities $\lambda_{i,j}$ for each entry. The distribution of the discrete Ridgelet transform $\mathcal{R}_{\mathbf{X}}$ of \mathbf{X} can be approximated by the difference of the scaled Poisson random variables as in Theorem 2.1.*

Proof. *Combining the results of Theorem 2.1 and Theorem 2.2, we get the result.* \square

2.5. Thresholding using Stein’s method

We denote the distribution of the difference of the scaled Poisson variables $W_{j,k} = \alpha_{j,k}^+ \tilde{W}_{j,k}^+ - \alpha_{j,k}^- \tilde{W}_{j,k}^-$ with $\mathcal{S}(\tilde{\lambda}_{j,k}^+, \alpha_{j,k}^+, \tilde{\lambda}_{j,k}^-, \alpha_{j,k}^-)$ and the distribution of the addition of the scaled Poisson variables $W_{j,k} = \alpha_{j,k}^+ \tilde{W}_{j,k}^+ - \alpha_{j,k}^- \tilde{W}_{j,k}^-$ with $\mathcal{Q}(\tilde{\lambda}_{j,k}^+, \alpha_{j,k}^+, \tilde{\lambda}_{j,k}^-, \alpha_{j,k}^-)$. Note that $\tilde{W}_{j,k}^+ \sim \text{Po}(\tilde{\lambda}_{j,k}^+)$ and $\tilde{W}_{j,k}^- \sim \text{Po}(\tilde{\lambda}_{j,k}^-)$. Let us assume that $w \sim \mathcal{S}(\tilde{\lambda}_{j,k}^+, \alpha_{j,k}^+, \tilde{\lambda}_{j,k}^-, \alpha_{j,k}^-)$ and $v \sim \mathcal{Q}(\tilde{\lambda}_{j,k}^+, \alpha_{j,k}^+, \tilde{\lambda}_{j,k}^-, \alpha_{j,k}^-)$. Considering the estimator $\hat{\Lambda}(w, v) = w + G(w, v)$ for the vector $[\lambda_{j,k}^+, \lambda_{j,k}^-]$, One can use Stein’s method to find the optimal threshold τ for soft thresholding $\hat{\Lambda}(w; \tau) = \text{sgn}(w) \cdot \max\{|w| - \tau, 0\}$ (Hirakawa & Wolfe, 2012).

3. Experiments

3.1. Verification of Noise Distribution

In this sub-section, we will present numerical experiments to verify the theoretically derived distributions of the Radon and ridgelet coefficients of Poisson-distributed images.

The assumed signal-dependent noise model is given by the relationship $\mathbf{X} = \mathbf{T}(\Lambda)$ in Equation (2). For the homogeneous case, we consider a constant-intensity 2D image corrupted with Poisson noise. We generate 1000 samples of the transforms and evaluate the distributional properties within transform coefficients. Baring the Poisson assumption in mind, we estimate the mean and variance of the transform coefficients and report on mean-variance ratios as well as the mean difference between the noisy and noiseless transforms. For the inhomogeneous case, we follow the same procedure but for 2D images with added structures.

3.1.1. DISTRIBUTION OF RADON TRANSFORM

This subsection reviews Poisson-noise generated images analysed in the Radon domain. Evaluations of the distributional properties of the noise were based on a discrete Radon transform implementing straightforward image rotations with $\theta \in [0, \pi)$. Figure 1 and 2 shows example images of the original and transforms noise in the homogeneous and inhomogeneous cases, respectively. The measured noise parameters shows that the transformed noise exhibits Poisson-characteristics such as equal mean and variance (mean variance ratios close to one); see Table 1. Furthermore, Figure 3 indicates a linear relationship between the noiseless pixel intensity and the variance of the noise images.

3.1.2. DISTRIBUTION OF RIDGELET TRANSFORM

This subsection reviews Poisson-noise generated images analysed in the ridgelet domain. Evaluations of the distributional properties of the noise were based on a discrete Radon transform implementing straightforward image rotations with $\theta \in [0, \pi)$ followed by a wavelet transform of the

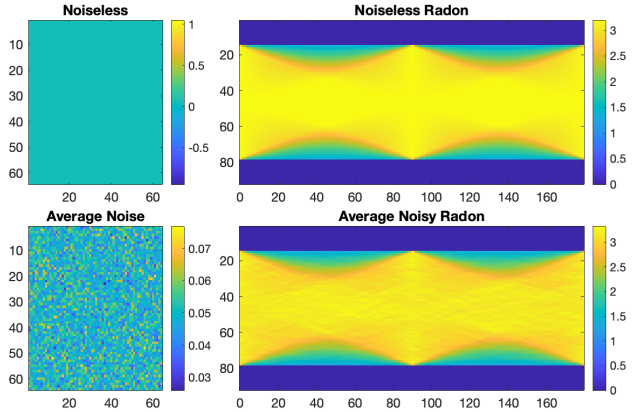


Figure 1. Visualisation of noiseless and average noisy Radon transforms of 1000 homogeneous Poisson-distributed images with intensity $\lambda = 0.05$.

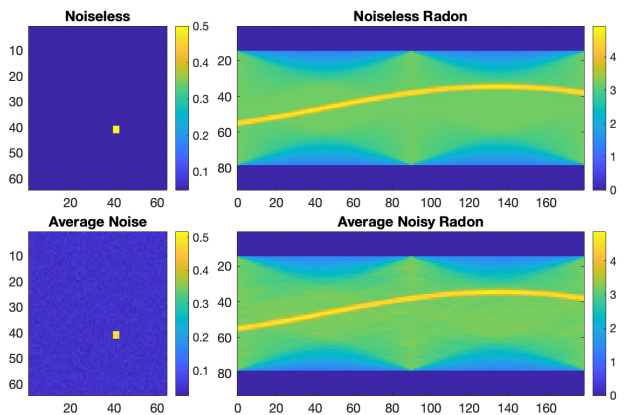


Figure 2. Visualisation of noiseless and average noisy Radon transforms of 1000 inhomogeneous Poisson-distributed images with intensity $\lambda = 0.05$ and added structures of intensity 10λ .

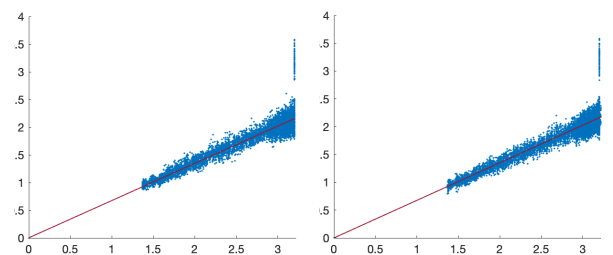


Figure 3. Noise analysis of the Poisson noise in the Radon domain showing noiseless pixel intensities versus noise variance for simulated Poisson-distributed images. Homogeneous case to the left, and inhomogeneous case to the right.

distributional properties of the noise were based on a discrete Radon transform implementing straightforward image rotations with $\theta \in [0, \pi)$ followed by a wavelet transform of the

Table 1. Estimated 95% confidence intervals for noise parameters of the Radon coefficients based on 1000 noisy Poisson images with intensity $\lambda = 0.05$. The inhomogeneous case includes additional structures of intensity 10λ .

<i>Homogeneous case</i>	
pixel mean	(1.950, 1.971)
pixel variance	(1.312, 1.326)
mean variance ratio	(1.033, 1.044)
mean difference (noisy vs noiseless)	(-0.005, -0.004)
<i>Inhomogeneous case</i>	
pixel mean	(1.994, 2.016)
Pixel variance	(1.348, 1.363)
mean variance ratio	(1.028, 1.039)
mean difference (noisy vs noiseless)	(-0.004, -0.003)

Radon projections using Haar wavelets on one levels. For both homogeneous and inhomogeneous cases, we evaluate the distributional properties on approximation and detail coefficients separately.

Figure 4 and 5 shows example images of the original and transforms noise in the homogeneous and inhomogeneous cases, respectively. The measured noise parameters shows that the transformed noise exhibits Poisson-characteristics such as equal mean and variance (mean variance ratios close to one) in the detail layer coefficients; see Table 2. The proportional relationship between the noiseless pixel intensity and the variance of the noise images is shown in Figure 6.

Table 2. Estimated 95% confidence intervals for noise parameters of the Radon coefficients based on Poisson images with intensity $\lambda = 0.05$. The inhomogeneous case includes additional structures of intensity 10λ .

<i>Homogeneous case</i>		
<i>Approximation coefficients</i>	pixel mean	(4.903, 5.143)
	pixel variance	(2.234, 2.347)
	mean variance ratio	(2.060, 2.124)
	mean difference (noisy vs noiseless)	(0.002, 0.009)
<i>Detail coefficients</i>	pixel mean	(0.724, 0.787)
	pixel variance	(0.439, 0.478)
	mean variance ratio	(1.179, 1.278)
	mean difference (noisy vs noiseless)	(0.639, 0.698)
<i>Inhomogeneous case</i>		
<i>Approximation coefficients</i>	pixel mean	(5.586, 5.764)
	pixel variance	(2.566, 2.653)
	mean variance ratio	(2.185, 2.200)
	mean difference (noisy vs noiseless)	(0.006, 0.012)
<i>Detail coefficients</i>	pixel mean	(0.715, 0.780)
	pixel variance	(0.440, 0.484)
	mean variance ratio	(1.132, 1.233)
	mean difference (noisy vs noiseless)	(0.603, 0.661)

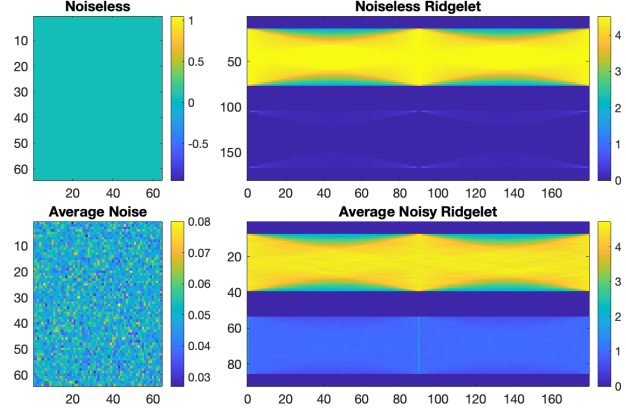


Figure 4. Visualisation of noiseless and average noisy ridgelet transforms based on 1-level Haar wavelets of 1000 homogeneous Poisson-distributed images with intensity $\lambda = 0.05$.

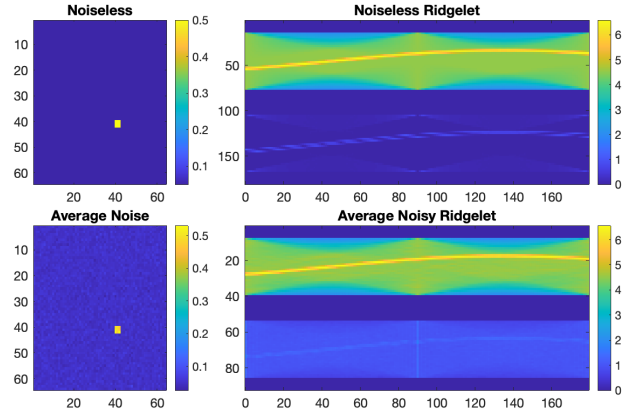


Figure 5. Visualisation of noiseless and average noisy ridgelet transforms based on 1-level Haar wavelets of 1000 inhomogeneous Poisson-distributed images with intensity $\lambda = 0.05$ and added structures of intensity 10λ .

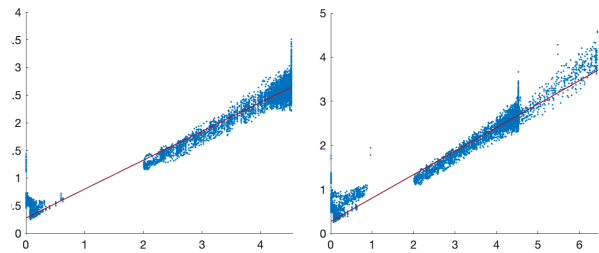


Figure 6. Noise analysis of the Poisson noise in the ridgelet domain based on 1-level Haar wavelets showing noiseless pixel intensities versus noise variance for simulated Poisson-distributed images. Homogeneous case to the left, and inhomogeneous case to the right.

3.2. Ridgelet Thresholding

In this subsection, we illustrate the potential efficiency of Poisson noise removal using the ridgelet-based shrinkage estimator described in Section 2.5. The estimator was implemented using Matlab’s efficient built in function for Radon transform with $\theta \in [0, \pi)$, followed by wavelet transform of the Radon projections using 1-level undecimated Haar wavelets. Parameter estimation for the corresponding shrinkage rules were based on empirical risk minimisation. Evaluation is based on relative mean square errors (MSE), structural similarity index measures (SSIM), and peak signal-to-noise ratios (PSNR) for noisy and thresholded images. We define the evaluation measures as:

$$MSE = \frac{1}{n} \sum_{i=0}^n (\hat{x}_i - x_i)^2$$

$$SSIM = l(\hat{x}, x)^\alpha c(\hat{x}, x)^\beta s(\hat{x}, x)^\gamma$$

$$PSNR = 10 \log \left(\frac{x_{max}^2}{MSE} \right)$$

where \hat{x} and x are the noisy and noiseless images, respectively, with n image pixels. The SSIM components for luminance (l), contrast (c), and structure (s) are calculated based on means μ , variance σ^2 and covariance $\sigma_{\hat{x}x}$ of the noisy and noiseless images as follows

$$l(\hat{x}, x) = \frac{2\mu_y\mu_{\hat{x}} + C_1}{\mu_x^2 + \mu_{\hat{x}}^2 + C_1}$$

$$c(\hat{x}, x) = \frac{2\sigma_y\sigma_{\hat{x}} + C_2}{\sigma_x^2 + \sigma_{\hat{x}}^2 + C_2}$$

$$s(\hat{x}, x) = \frac{\sigma_{x\hat{x}} + C_3}{\sigma_y\sigma_{\hat{x}} + C_3}$$

where C_1, C_2 and C_3 are constants dependent of the dynamic range (L) of the images such that $C_1 = (0.01L)^2$, $C_2 = (0.03L)^2$ and $C_3 = C_2/2$. For simplicity, we let $\alpha = \beta = \gamma = 1$.

We consider a simple 2D image with constant-intensity background and added structures following the inhomogeneous case in Section 3.1. The resulting MSE, SSIM, and PSNR for 1000 noisy and denoised images are shown in Table 3, and a visual comparison can be seen in Figure 7.

Table 3. Estimated average (standard deviation) relative mean squared error (MSE), structural similarity index measure (SSIM), and peak signal-to-noise ratio (PSNR) based on 1000 samples of noisy and denoised data.

	Noisy	Denoised
MSE	0.820 (0.039)	$8.383 \cdot 10^4 (4.434 \cdot 10^5)$
SSIM	0.002 ($1.289 \cdot 10^4$)	66.618 (0.010)
PSNR	49.00 (0.204)	78.903 (0.228)

To illustrate a potential area of application, we also consider ridgelet thresholding of Poisson data originating from PET

measurements represented by 2D sinograms. The sinogram pixel values are considered as the true underlying intensity function of interest. We report on noise level characterisation and denoising efficiency in terms of MSE and SSIM. Implementations were set using undecimated Haar wavelets on 3 levels. The resulting MSE, SSIM, and PSNR for 1000 noisy and denoised images are shown in Table 4, as well as a visual comparison in Figure 8.

Table 4. Estimated average (standard deviation) relative mean squared error (MSE), structural similarity index measure (SSIM), and peak signal-to-noise ratio (PSNR) based on 1000 samples of noisy and denoised PET measurements.

	Noisy	Denoised
MSE	60.381 (0.116)	7.655 (0.055)
SSIM	0.146 (0.001)	0.352 (0.005)
PSNR	30.322 (0.008)	39.291 (0.031)

4. Discussion

In this study, we have investigated the distributional properties of noisy Poisson-distributed images in the Radon and wavelet domains in order to propose a proper thresholding scheme for noise removal in the ridgelet domain. We have shown, theoretically and experimentally, that the ridgelet transform preserves the Poisson distribution properties of the noise. This revelation is pivotal as it steers clear the pathway for leveraging the inherent characteristics of Poisson noise in the denoising process. Our theoretical framework proposes an adaptive thresholding approach in the ridgelet domain, guided by Stein’s method. This approach not only aligns with the nature of Poisson noise but also opens up avenues for more refined denoising techniques.

The experimental part of our study brings to light several intriguing aspects. Our noise analysis experiments revealed a tendency for underdispersion in the noise distribution. A plausible explanation for this could be the aggregated effect of pixel summation in the transforms, potentially elevating the mean more significantly than the variance. This might also imply a smoothing effect inherent in the summation process. Furthermore, although transform coefficients in the radon domain indicate a linear noise model, this is not the case for ridgelet coefficients. Using wavelet decomposition on one level indicates that detail coefficients follow a linear noise model.

The theoretical framework we have established lays the groundwork for developing a comprehensive denoising algorithm tailored for images corrupted with Poisson noise. The denoising results, as presented in our experiments, illustrate the potential of our proposed ridgelet thresholding technique. The immediate goal is to refine the ridgelet denoising technique, harnessing its potential to exploit Poisson

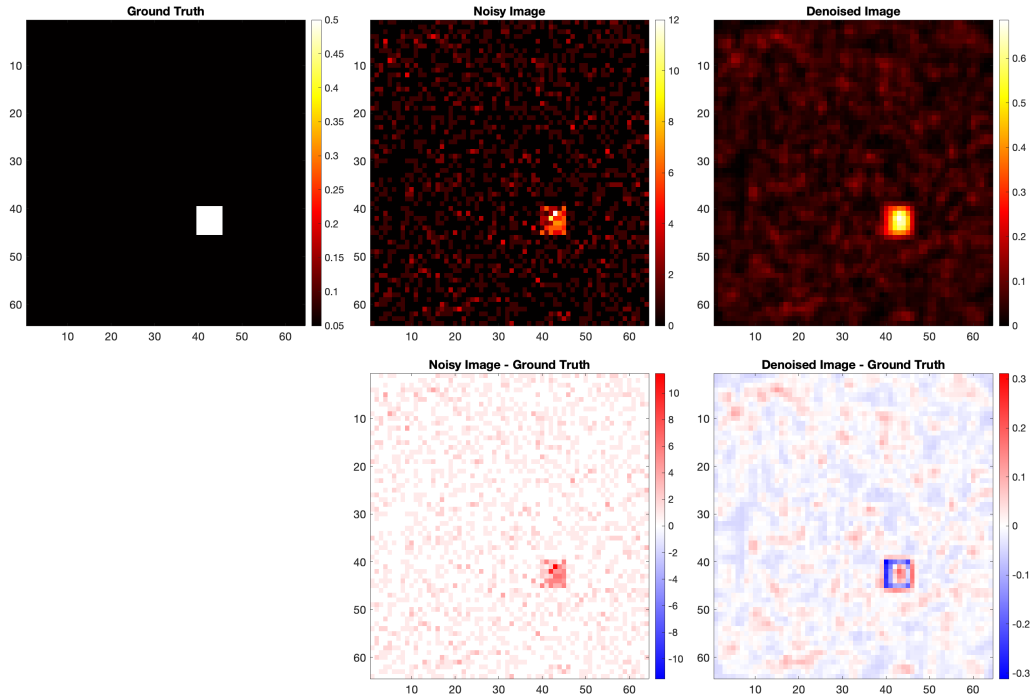


Figure 7. Thresholding experiments for Poisson-corrupted images showing the noiseless ground truth, the noisy image, and the denoised image based on ridgelet thresholding. Difference images between noisy or denoised and ground truth are shown on the bottom row.

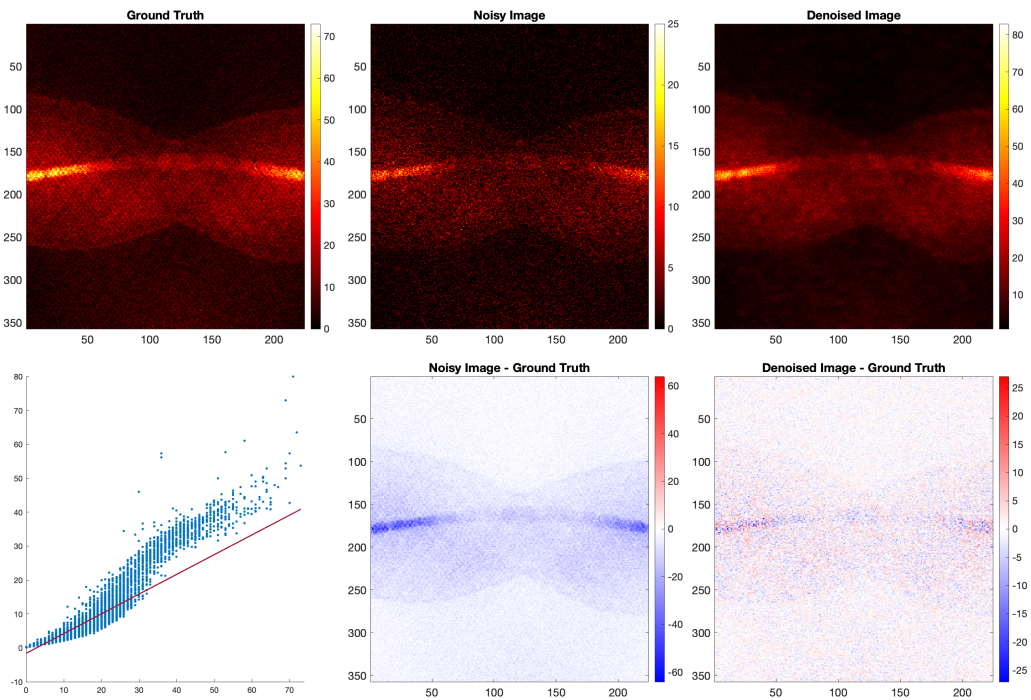


Figure 8. Thresholding experiments for Poisson-corrupted images showing the noiseless ground truth, the noisy image, and the denoised image based on ridgelet thresholding. Difference images between noisy or denoised and ground truth are shown on the bottom row. Noise analysis comparing noiseless pixel intensities versus noise variance for denoised images are shown at the bottom left.

distributional properties effectively. Furthermore, the slight deviations observed in experimental patterns from our theoretical predictions highlight areas for future research. Delving deeper into these anomalies could unveil new insights into the behaviour of Poisson noise under various transforms and lead to even more robust denoising strategies.

In conclusion, our study represents a significant step in understanding and tackling Poisson noise in images through the lens of the ridgelet transform. The theoretical and experimental findings open up the development of advanced denoising techniques that are both effective and aligned with the intrinsic properties of Poisson noise. As we explore this domain, the horizon of possibilities in image processing and computer vision widens.

Funding

This work is supported by the Swedish Research Council (340-2013-5342).

References

- Anscombe, F. J. The transformation of Poisson, binomial and negative-binomial data. *Biometrika*, 35(3-4):246–254, 12 1948. ISSN 0006-3444. doi: 10.1093/biomet/35.3-4.246.
- Azzari, L. and Foi, A. Variance stabilization for noisy+ estimate combination in iterative poisson denoising. *IEEE signal processing letters*, 23(8):1086–1090, 2016. doi: 10.1109/LSP.2016.2580600.
- Bohm, G. and Zech, G. Statistics of weighted Poisson events and its applications. *Nuclear Instruments and Methods in Physics Research Section A: Accelerators, Spectrometers, Detectors and Associated Equipment*, 748:1–6, 2014.
- Brady, M. L. A fast discrete approximation algorithm for the Radon transform. *SIAM Journal on Computing*, 27(1):107–119, 1998.
- Candès, E. J. and Donoho, D. L. Ridgelets: A key to higher-dimensional intermittency? *Philosophical Transactions of the Royal Society of London. Series A: Mathematical, Physical and Engineering Sciences*, 357(1760):2495–2509, 1999. doi: 10.1098/rsta.1999.0444.
- Carre, P. and Andres, E. Discrete analytical ridgelet transform. *Signal processing*, 84(11):2165–2173, 2004. doi: 10.1016/j.sigpro.2004.07.009.
- Chan, T., Marquina, A., and Mulet, P. High-order total variation-based image restoration. *SIAM Journal on Scientific Computing*, 22(2):503–516, 2000. doi: 10.1137/S1064827598344169.
- Charles, C. and Rasson, J.-P. Wavelet denoising of Poisson-distributed data and applications. *Computational statistics & data analysis*, 43(2):139–148, 2003. doi: 10.1016/S0167-9473(02)00208-6.
- Chen, G. and Kégl, B. Image denoising with complex ridgelets. *Pattern Recognition*, 40(2):578–585, 2007. doi: 10.1016/j.patcog.2006.04.039.
- Chen, Y. and Pock, T. Trainable nonlinear reaction diffusion: A flexible framework for fast and effective image restoration. *IEEE transactions on pattern analysis and machine intelligence*, 39(6):1256–1272, 2016. doi: 10.1109/TPAMI.2016.2596743.
- Dabov, K., Foi, A., Katkovnik, V., and Egiazarian, K. Image denoising by sparse 3-D transform-domain collaborative filtering. *IEEE Transactions on image processing*, 16(8):2080–2095, 2007. doi: 10.1109/TIP.2007.901238.
- Do, M. N. and Vetterli, M. Orthonormal finite ridgelet transform for image compression. In *Proceedings 2000 International Conference on Image Processing (Cat. No. 00CH37101)*, volume 2, pp. 367–370. IEEE, 2000. doi: 10.1109/ICIP.2000.899394.
- Dong, W., Shi, G., and Li, X. Nonlocal image restoration with bilateral variance estimation: A low-rank approach. *IEEE transactions on image processing*, 22(2):700–711, 2012. doi: 10.1109/TIP.2012.2221729.
- Feng, W., Qiao, P., and Chen, Y. Fast and accurate poisson denoising with trainable nonlinear diffusion. *IEEE Transactions on Cybernetics*, 48(6):1708–1719, 2017. doi: 10.1109/TCYB.2017.2713421.
- Figueiredo, M. A. and Bioucas-Dias, J. M. Restoration of Poissonian images using alternating direction optimization. *IEEE transactions on Image Processing*, 19(12):3133–3145, 2010. doi: 10.1109/TIP.2010.2053941.
- Fryzlewicz, P. and Nason, G. P. A Haar-Fisz algorithm for Poisson intensity estimation. *Journal of computational and graphical statistics*, pp. 621–638, 2004.
- Giryes, R. and Elad, M. Sparsity-based Poisson denoising with dictionary learning. *IEEE Transactions on Image Processing*, 23(12):5057–5069, 2014. doi: 10.1109/TIP.2014.2362057.
- Götz, W. and Druckmüller, H. A fast digital Radon transform—An efficient means for evaluating the Hough transform. *Pattern Recognition*, 29(4):711–718, 1996.
- Hasinoff, S. W. Photon, Poisson Noise. *Computer Vision, A Reference Guide*, 4(16):1, 2014.

- Hirakawa, K. and Wolfe, P. J. Skellam Shrinkage: Wavelet-Based Intensity Estimation for Inhomogeneous Poisson Data. *IEEE Transactions on Information Theory*, 58(2): 1080–1093, 2012. doi: 10.1109/TIT.2011.2165933.
- Jensen, A. and la Cour-Harbo, A. *Ripples in mathematics: the discrete wavelet transform*. Springer Science & Business Media, 2001.
- Kolaczyk, E. D. A wavelet shrinkage approach to tomographic image reconstruction. *Journal of the American Statistical Association*, pp. 1079–1090, 1996.
- Kolaczyk, E. D. Wavelet shrinkage estimation of certain Poisson intensity signals using corrected thresholds. *Statistica Sinica*, pp. 119–135, 1999.
- Kumwilaisak, W., Piriyaatharawet, T., Lasang, P., and Thatphithakkul, N. Image denoising with deep convolutional neural and multi-directional long short-term memory networks under Poisson noise environments. *IEEE Access*, 8:86998–87010, 2020. doi: 10.1109/ACCESS.2020.2991988.
- Lantéri, H. and Theys, C. Restoration of astrophysical images—the case of Poisson data with additive Gaussian noise. *EURASIP Journal on Advances in Signal Processing*, 2005:1–14, 2005. doi: 10.1155/ASP.2005.2500.
- Le, T., Chartrand, R., and Asaki, T. J. A variational approach to reconstructing images corrupted by Poisson noise. *Journal of mathematical imaging and vision*, 27(3):257–263, 2007. doi: 10.1007/s10851-007-0652-y.
- Liang, H., Liu, R., Wang, Z., Ma, J., and Tian, X. Variational Bayesian deep network for blind Poisson denoising. *Pattern Recognition*, 143:109810, 2023. doi: 10.1016/j.patcog.2023.109810.
- Liu, Y.-X., Law, N.-F., and Siu, W. C. Patch based image denoising using the finite ridgelet transform for less artifacts. *Journal of Visual Communication and Image Representation*, 25(5):1006–1017, 2014. doi: 10.1016/j.jvcir.2014.02.018.
- Lu, H., Kim, Y., and Anderson, J. Improved Poisson intensity estimation: denoising application using Poisson data. *IEEE Transactions on Image Processing*, 13(8): 1128–1135, 2004. doi: 10.1109/TIP.2003.822606.
- Luisier, F., Vonesch, C., Blu, T., and Unser, M. Fast interscale wavelet denoising of Poisson-corrupted images. *Signal processing*, 90(2):415–427, 2010. doi: 10.1016/j.sigpro.2009.07.009.
- Press, W. J. Discrete Radon transform has an exact, fast inverse and generalizes to operations other than sums along lines. *Proceedings of the National Academy of Sciences*, 103(51):19249–19254, 2006. doi: 10.1073/pnas.0609228103.
- Priego, B., Duro, R. J., and Chanussot, J. 4DCAF: A temporal approach for denoising hyperspectral image sequences. *Pattern Recognition*, 72:433–445, 2017. doi: 10.1016/j.patcog.2017.07.023.
- Remez, T., Litany, O., Giryas, R., and Bronstein, A. M. Deep convolutional denoising of low-light images. *arXiv preprint arXiv:1701.01687*, 2017. doi: 10.48550/arXiv.1701.01687.
- Rudin, L. I., Osher, S., and Fatemi, E. Nonlinear total variation based noise removal algorithms. *Physica D: nonlinear phenomena*, 60(1-4):259–268, 1992. doi: 10.1016/0167-2789(92)90242-F.
- Thanh, D. and Dvoenko, S. A denoising of biomedical images. *The International Archives of the Photogrammetry, Remote Sensing and Spatial Information Sciences*, 40:73–78, 2015. doi: 10.5194/isprsarchives-XL-5-W6-73-2015.
- Thanh, D., Surya, P., et al. A review on ct and x-ray images denoising methods. *Informatica*, 43(2), 2019. doi: 10.31449/inf.v43i2.2179.
- Timmermann, K. E. and Nowak, R. D. Multiscale modeling and estimation of Poisson processes with application to photon-limited imaging. *IEEE Transactions on Information Theory*, 45(3):846–862, 1999. doi: 10.1109/18.761328.
- Vardi, Y., Shepp, L. A., and Kaufman, L. A statistical model for positron emission tomography. *Journal of the American statistical Association*, pp. 8–20, 1985. doi: 10.2307/2288030.
- Yang, S., Min, W., Zhao, L., and Wang, Z. Image noise reduction via geometric multiscale ridgelet support vector transform and dictionary learning. *IEEE Transactions on Image Processing*, 22(11):4161–4169, 2013. doi: 10.1109/TIP.2013.2271114.
- Zhang, B., Fadili, J. M., and Starck, J.-L. Wavelets, ridgelets, and curvelets for Poisson noise removal. *IEEE Transactions on image processing*, 17(7):1093–1108, 2008. doi: 10.1109/TIP.2008.924386.
- Zhang, J., Zhao, L., and Wei, Z. Poisson-Skellam distribution based regularization conditional random field method for photon-limited Poisson image denoising. *Signal Processing*, 188:108165, 2021. doi: 10.1016/j.sigpro.2021.108165.
- Zhang, M., Zhang, F., Liu, Q., and Wang, S. VST-Net: Variance-stabilizing transformation inspired network for Poisson denoising. *Journal of Visual Communication and Image Representation*, 62:12–22, 2019a. doi: 10.1016/j.jvcir.2019.04.011.

Zhang, M., Zhang, F., Liu, Q., and Wang, S. VST-Net: Variance-stabilizing transformation inspired network for Poisson denoising. *Journal of Visual Communication and*

Image Representation, 62:12–22, 2019b. doi: 10.1016/j.jvcir.2019.04.011.